

# Supporting information

## **In-situ observed local structural distortions boost solar water splitting in hematite**

*Cheng Lu,<sup>#a</sup> Zihou Jiang,<sup>#a</sup> Jiabin Xu,<sup>b</sup> Shuo Li,<sup>c</sup> Yong Feng,<sup>a</sup> Bai Xu,<sup>a</sup> Gongcheng Liu,<sup>a</sup> Ye  
Zhu,<sup>a</sup> Kun Feng,<sup>a</sup> and Jun Zhong<sup>\*a</sup>*

<sup>a</sup> Institute of Functional Nano and Soft Materials Laboratory (FUNSOM), Jiangsu Key  
Laboratory of Advanced Negative Carbon Technologies, Soochow University, Suzhou 215123,  
China

<sup>b</sup> Department of Chemistry and Soochow-Western Centre for Synchrotron Radiation Research  
University of Western Ontario, London, Ontario, N6A 5B7, Canada

<sup>c</sup> State Key Laboratory of Radiation Medicine and Protection, School for Radiological and  
Interdisciplinary Sciences (RAD-X) and Collaborative Innovation Center of Radiation  
Medicine of Jiangsu Higher Education Institutions, Soochow University, Suzhou 215123,  
China.

<sup>#</sup>These authors contributed equally.

\*Address correspondence to [jzhong@suda.edu.cn](mailto:jzhong@suda.edu.cn).

## Photoelectrochemical measurements

The PEC tests were carried out using a CHI660D workstation and a standard three-electrode system in a 1 M NaOH solution, illuminated by simulated sunlight AM 1.5 G (100 mW cm<sup>-2</sup>) over a test area of approximately 0.1 cm<sup>2</sup>. Photoelectrochemical impedance spectroscopy (PEIS) measurements were conducted under light conditions by applying a 10 mV AC perturbation in the frequency range of 0.1 Hz-10<sup>5</sup> Hz at 1.0 V<sub>RHE</sub>, and Mott-Schottky tests were performed at 1 kHz under dark conditions. The carrier concentration (N<sub>d</sub>) was subsequently calculated according to the following equation:

$$N_d = \left( \frac{2}{e_0 \varepsilon \varepsilon_0} \right) \left[ \frac{d \left( \frac{1}{C^2} \right)}{dV} \right]^{-1}$$

where  $\varepsilon$  is the dielectric constant of  $\alpha$ -Fe<sub>2</sub>O<sub>3</sub>,  $\varepsilon_0$  represents the vacuum permittivity (8.854×10<sup>-14</sup> F cm<sup>-1</sup>),  $e_0$  is the elementary charge (1.602×10<sup>-19</sup> C), and C is the space charge layer capacitance (F cm<sup>-2</sup>).<sup>1</sup> In this work the surface roughness and nanorod dimensions of the photoanode are also considered, the calculation of carrier concentration incorporates the surface roughness factor (A<sub>s</sub>):<sup>2</sup>

$$N_d = \left( \frac{2}{e_0 \varepsilon \varepsilon_0} \right) \left[ \frac{d \left( \frac{A_s}{C^2} \right)}{dV} \right]^{-1}$$

Furthermore, the relationship between the surface roughness factor and the specific surface area of the photoanode has been expressed by this formula :

$$SSA = \frac{A_s}{\rho t}$$

where SSA is the specific surface area (m<sup>2</sup> g<sup>-1</sup>),  $\rho$  is the density of  $\alpha$ -Fe<sub>2</sub>O<sub>3</sub>, t is the (average)

thickness of the film (set as 250 nm),  $A_s$  is the surface roughness factor (dimensionless).

The efficiencies for surface charge injection ( $\eta_{surf}$ ) and bulk charge separation ( $\eta_{bulk}$ ) were derived from:

$$\eta_{surf} = \frac{J_{H_2O}}{J_{H_2O_2}} \times 100\%$$

$$\eta_{bulk} = \frac{J_{H_2O_2}}{J_{abs}} \times 100\%$$

where  $J_{H_2O}$  and  $J_{H_2O_2}$  are the photocurrent densities ( $\text{mA cm}^{-2}$ ) measured in 1 M NaOH with and without 0.5 M  $H_2O_2$ , respectively;  $J_{abs}$  is the calculated photocurrent density ( $\text{mA cm}^{-2}$ ) assuming complete conversion of absorbed photons.<sup>1</sup>

$$J_{abs} = \int_{\lambda_1}^{\lambda_2} \frac{\lambda}{1240} P_{abs}(\lambda) d\lambda \left( \frac{\text{mW}}{\text{cm}^2} \right)$$

where  $J_{abs}$  is the integrated current density ( $\text{mA cm}^{-2}$ ),  $P_{abs}$  is power of light actually absorbed by the photoanode ( $\text{mW cm}^{-2} \text{ nm}^{-1}$ ).<sup>3</sup>

By applying the equation to the impedance values obtained from fitting the PEIS data, the charge transfer efficiency ( $\eta_{trans}$ ) can be determined.

$$\eta_{trans} \approx \frac{R_{trap}}{R_{trap} + R_{ct}}$$

where  $R_{trap}$  is the bulk resistance and  $R_{ct}$  is the interfacial charge transfer resistance of the equivalent circuit model in Figure 2d.<sup>3</sup>

The incident photon-to-current conversion efficiency (IPCE) at 1.23  $V_{RHE}$ , across 300-650 nm, was calculated as:

$$IPCE = \frac{1240}{\lambda} \times \frac{J_{light}}{P_{light}} \times 100\%$$

where  $J_{\text{light}}$  is the photocurrent density ( $\text{mA cm}^{-2}$ ),  $\lambda$  is the wavelength (nm), and  $P_{\text{light}}$  denotes the light intensity at the corresponding wavelength ( $\text{mW cm}^{-2} \text{ nm}^{-1}$ ).<sup>4</sup>

The ABPE (applied bias photon-to-current efficiency) was evaluated using the equation below.:

$$ABPE = \frac{J \times (1.23 - E)}{P} \times 100\%$$

where  $J$  is the photocurrent density ( $\text{mA cm}^{-2}$ ),  $E$  is the applied potential, and  $P$  is the incident power density.<sup>5</sup>

The electrochemically active surface area (ECSA) was evaluated by determining the double-layer capacitance ( $C_{\text{dl}}$ ) through cyclic voltammetry (CV) conducted at scan rates from 20 to 100  $\text{mV s}^{-1}$  in 20  $\text{mV s}^{-1}$  intervals. The value of  $C_{\text{dl}}$  was obtained from the slope of the linear fit between capacitive current density and scan rate.<sup>5</sup>

The carrier lifetimes are calculated by:

$$\tau_n = -\frac{\kappa_B T}{e} \left( \frac{dOCP}{dt} \right)^{-1}$$

where  $\tau_n$ ,  $\kappa_B$ ,  $T$ ,  $e$ , and  $\frac{dOCP}{dt}$  are the carrier lifetime, Boltzmann's constant, temperature (K), charge of single electron, and derivative of the OCP transient decay, respectively.<sup>3</sup>

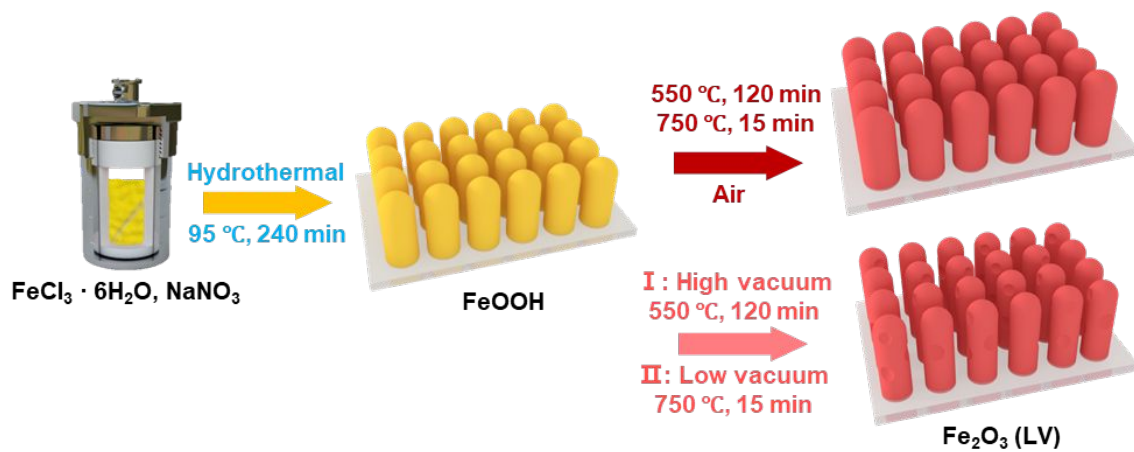


**Figure S1.** Schematic illustration of the synthesis processes for  $\text{Fe}_2\text{O}_3$  and  $\text{Fe}_2\text{O}_3$  (LV).

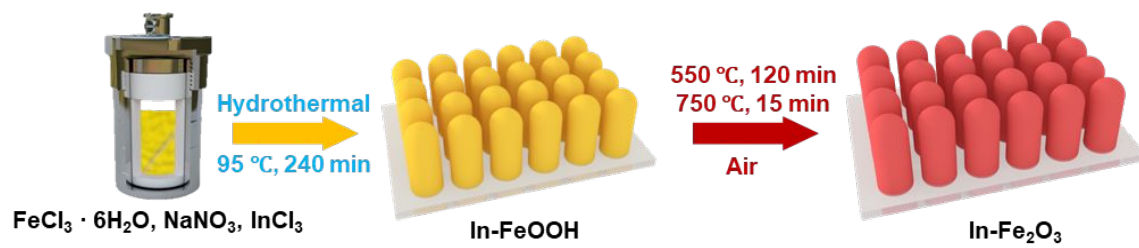


**Figure S2.** Schematic illustration of the synthesis processes for In-Fe<sub>2</sub>O<sub>3</sub>.

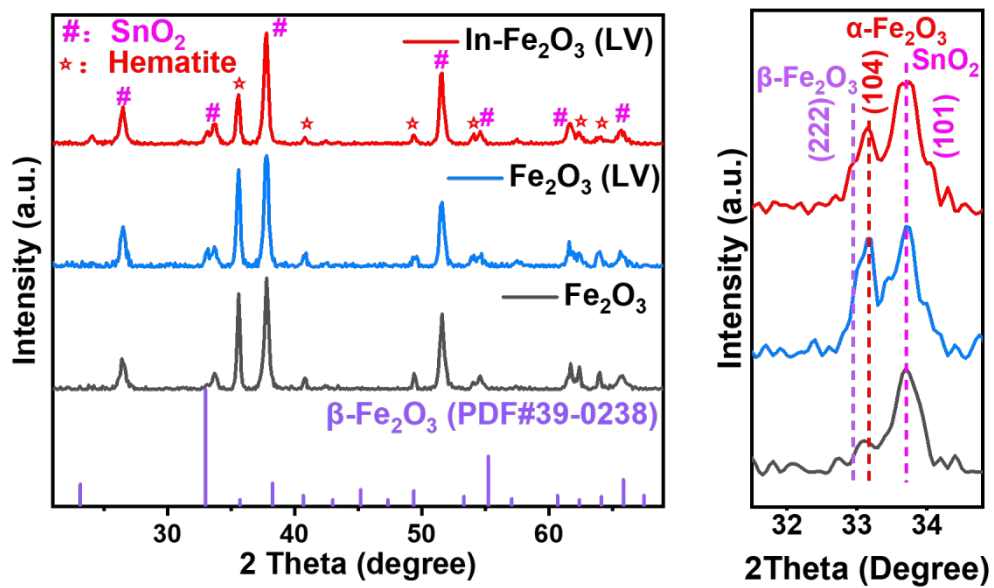


**Figure S3.** XRD patterns of Fe<sub>2</sub>O<sub>3</sub>, Fe<sub>2</sub>O<sub>3</sub> (LV), In- Fe<sub>2</sub>O<sub>3</sub> (LV) with the reference data of β-Fe<sub>2</sub>O<sub>3</sub>.

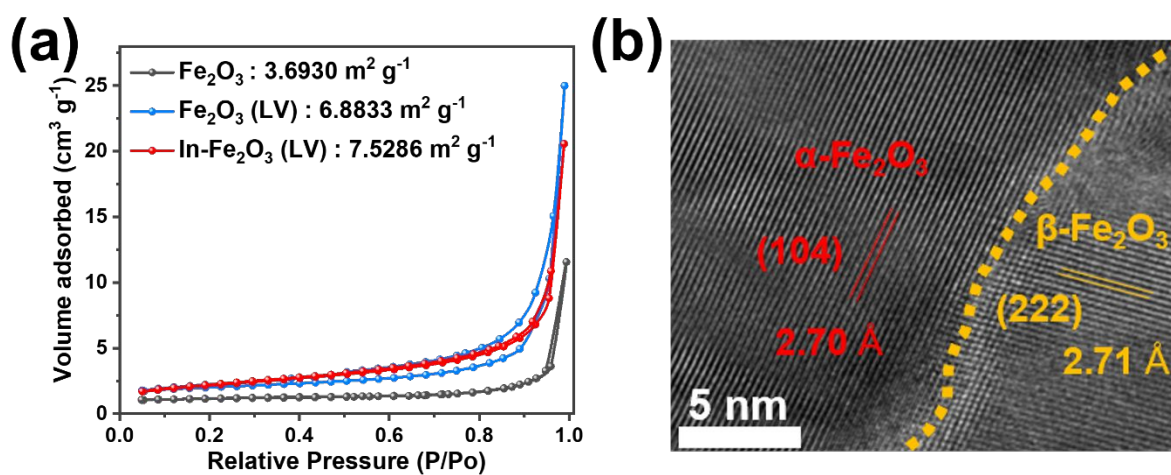


**Figure S4.** (a) N<sub>2</sub> adsorption-desorption isotherms and the corresponding BET values of Fe<sub>2</sub>O<sub>3</sub>, Fe<sub>2</sub>O<sub>3</sub> (LV) and In-Fe<sub>2</sub>O<sub>3</sub> (LV), respectively. (b) HRTEM images of In-Fe<sub>2</sub>O<sub>3</sub> (LV).

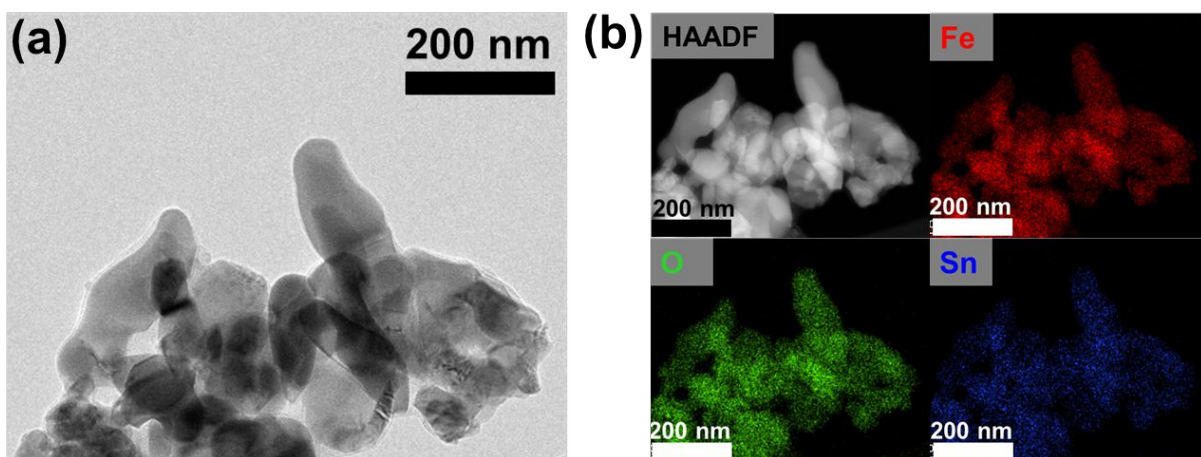


**Figure S5.** (a) TEM image and (b) elemental mappings of  $\text{Fe}_2\text{O}_3$ , respectively.

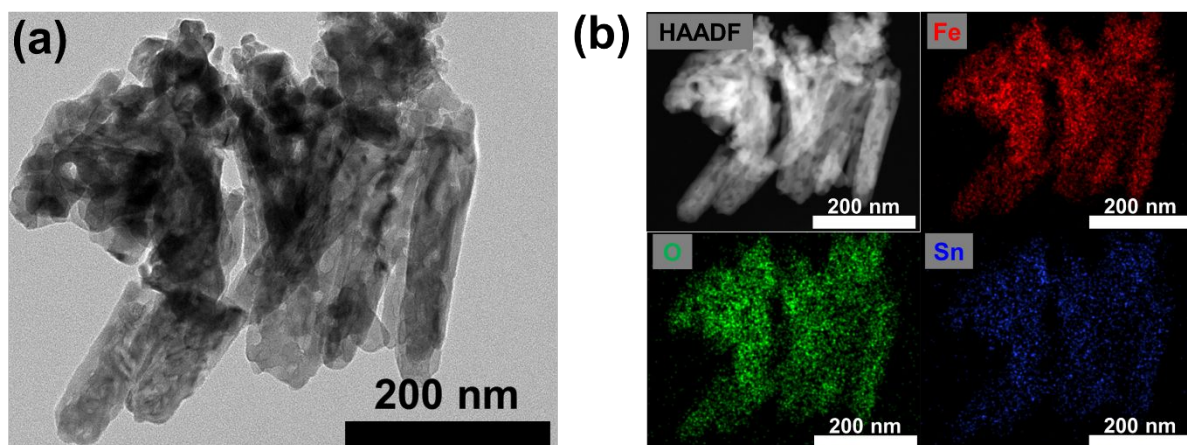


**Figure S6.** (a) TEM image and (b) elemental mappings of  $\text{Fe}_2\text{O}_3$  (LV), respectively.

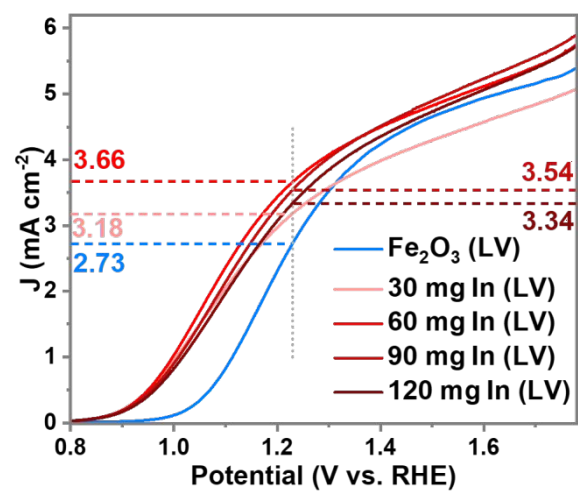


**Figure S7.** *J-V* curves of Fe<sub>2</sub>O<sub>3</sub> (LV) with different concentrations of InCl<sub>3</sub> solution (30, 60, 90, 120 mg mL<sup>-1</sup>).

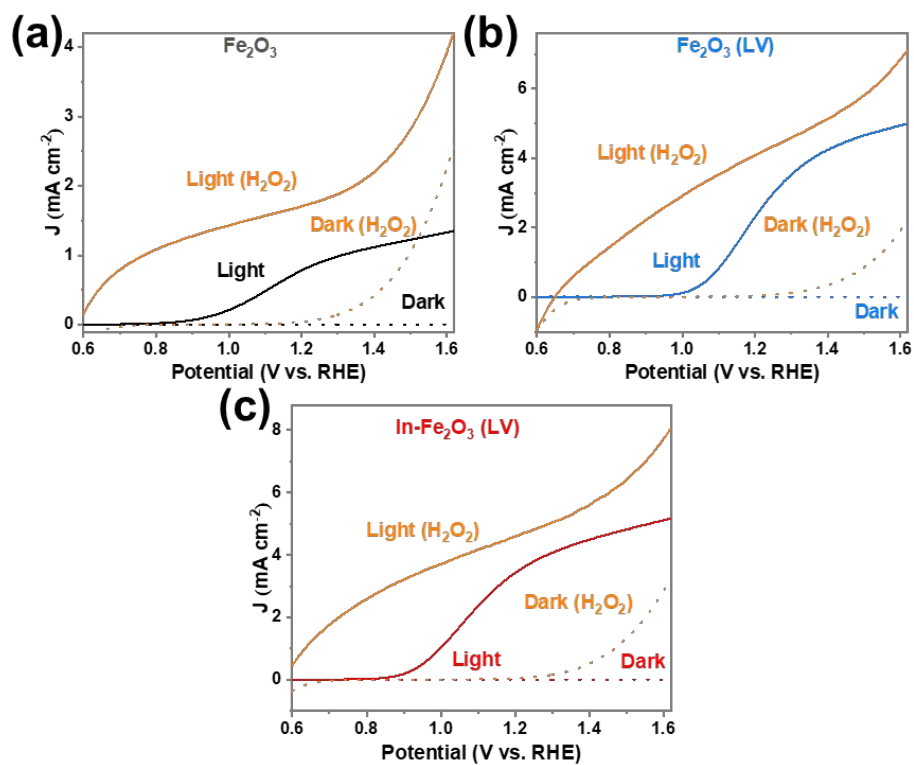


**Figure S8.**  $J$ - $V$  curves with and without H<sub>2</sub>O<sub>2</sub> (0.5 M) for (a) Fe<sub>2</sub>O<sub>3</sub>, (b) Fe<sub>2</sub>O<sub>3</sub> (LV) and (c) In-Fe<sub>2</sub>O<sub>3</sub> (LV), respectively.

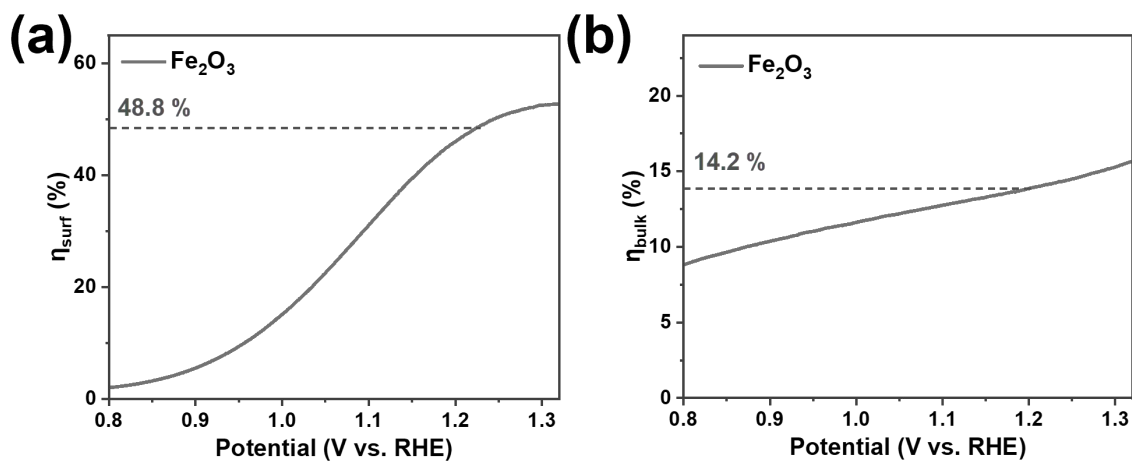


**Figure S9.** (a) Surface charge separation efficiency ( $\eta_{\text{surf}}$ ) and (b) bulk charge separation efficiency ( $\eta_{\text{bulk}}$ ) of Fe<sub>2</sub>O<sub>3</sub>.

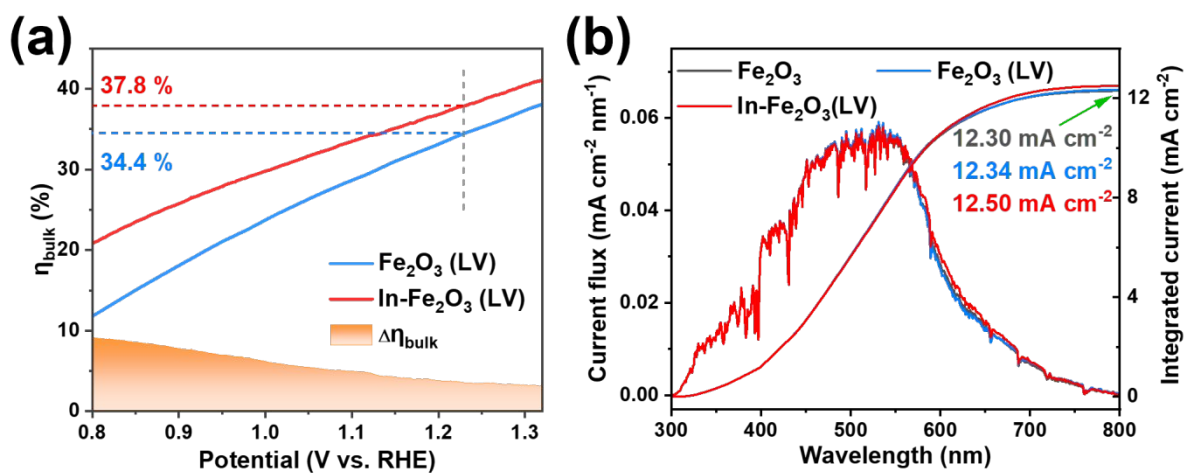


**Figure S10.** (a) Bulk charge separation efficiencies ( $\eta_{\text{bulk}}$ ) and  $\Delta\eta_{\text{bulk}}$  of  $\text{Fe}_2\text{O}_3$  (LV) and  $\text{In-Fe}_2\text{O}_3$  (LV). (b) Calculated current density flux and integrated current density ( $J_{\text{abs}}$ ) of  $\text{In-Fe}_2\text{O}_3$  (LV),  $\text{Fe}_2\text{O}_3$  (LV) and  $\text{Fe}_2\text{O}_3$ .

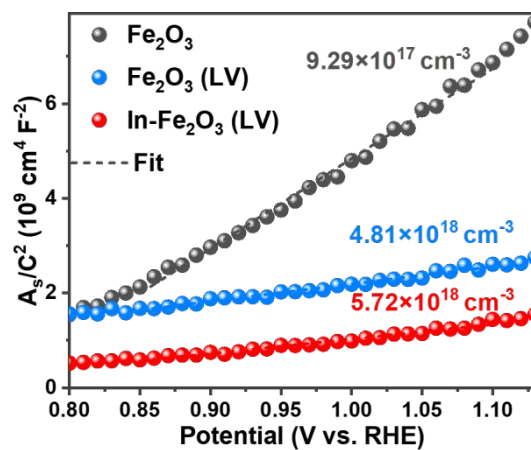


**Figure S11.** Mott-Schottky plots and  $N_d$  values of  $\text{Fe}_2\text{O}_3$ ,  $\text{Fe}_2\text{O}_3$  (LV) and  $\text{In-Fe}_2\text{O}_3$  (LV).

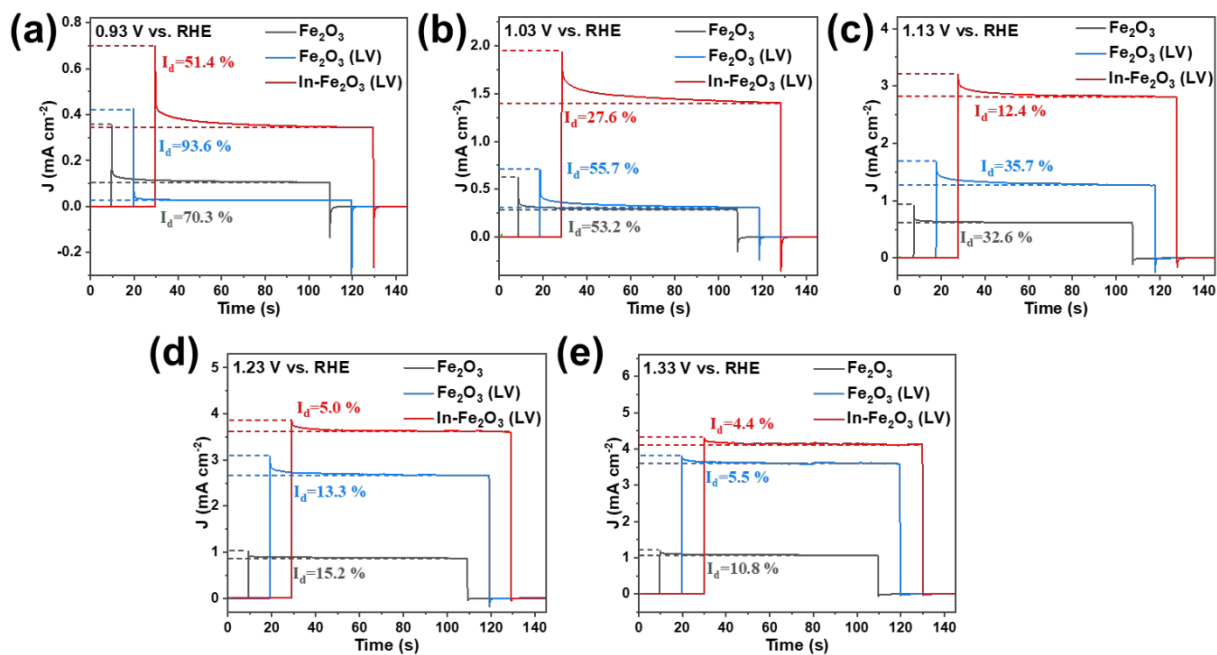


**Figure S12.** (a-e) Transient photocurrent densities of Fe<sub>2</sub>O<sub>3</sub>, Fe<sub>2</sub>O<sub>3</sub> (LV) and In-Fe<sub>2</sub>O<sub>3</sub> (LV) at 0.93, 1.03, 1.13, 1.23 and 1.33 V<sub>RHE</sub>, respectively.

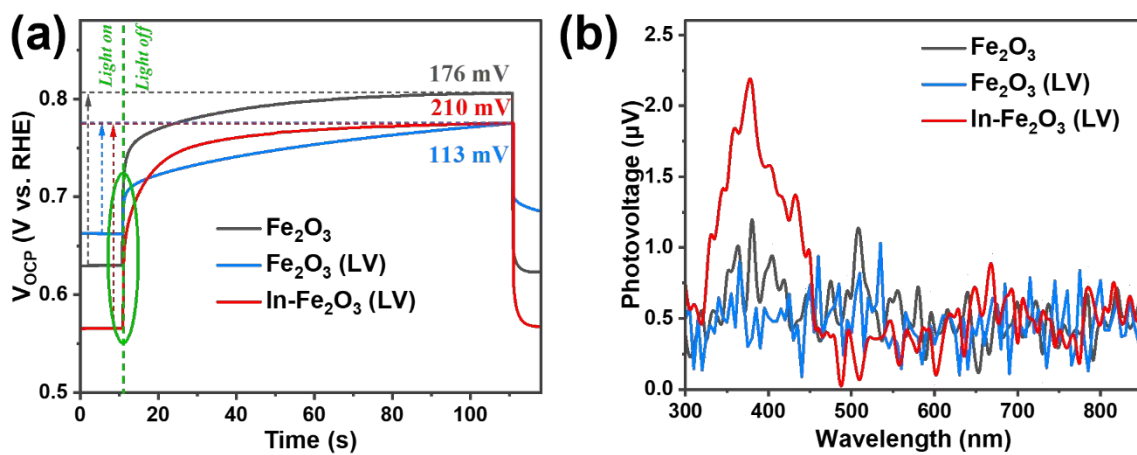


**Figure S13.** (a) OCP transient decay curves and (b) SPV curves of  $\text{Fe}_2\text{O}_3$ ,  $\text{Fe}_2\text{O}_3$  (LV) and  $\text{In-Fe}_2\text{O}_3$  (LV).

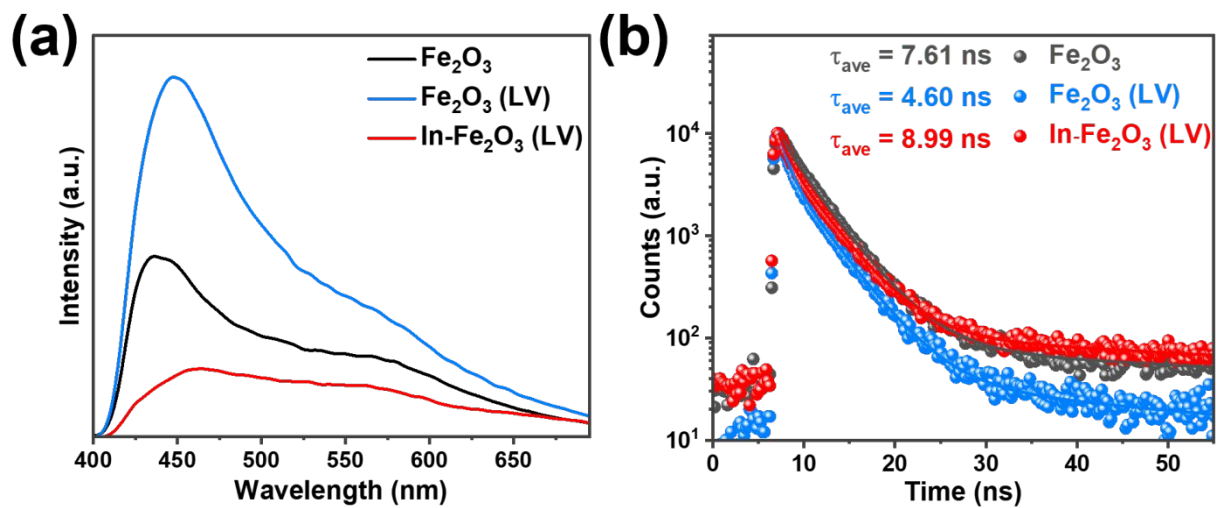


**Figure S14.** (a) Steady-state PL and (b) TRPL of Fe<sub>2</sub>O<sub>3</sub>, Fe<sub>2</sub>O<sub>3</sub> (LV) and In-Fe<sub>2</sub>O<sub>3</sub> (LV).

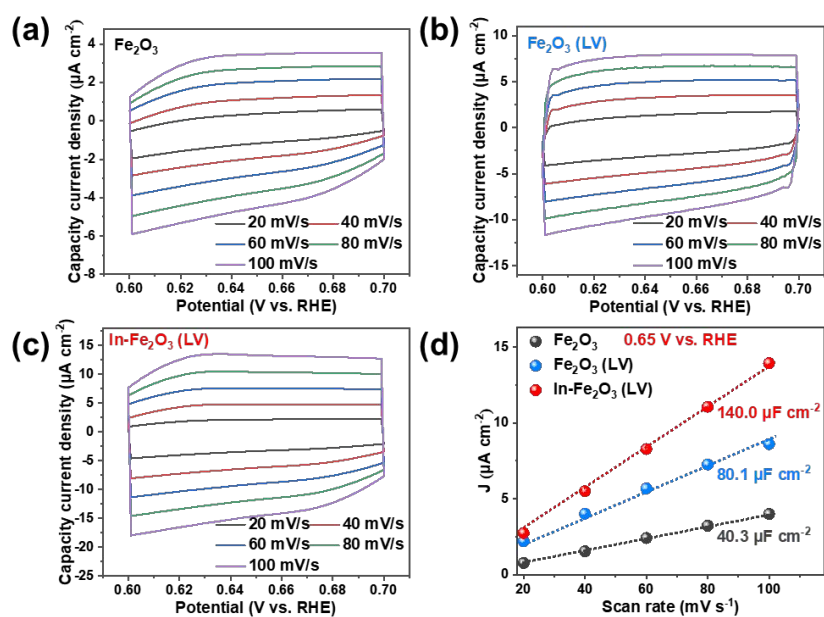


**Figure S15.** CV curves of (a)  $\text{Fe}_2\text{O}_3$ , (b)  $\text{Fe}_2\text{O}_3$  (LV) and (c)  $\text{In-Fe}_2\text{O}_3$  (LV) measured at different scan rates (20, 40, 60, 80 and 100  $\text{mV s}^{-1}$ ). (d) Linear relationship of the capacity currents at  $0.65 \text{ V}_{\text{RHE}}$  against the scan rates for  $\text{Fe}_2\text{O}_3$ ,  $\text{Fe}_2\text{O}_3$  (LV) and  $\text{In-Fe}_2\text{O}_3$  (LV).

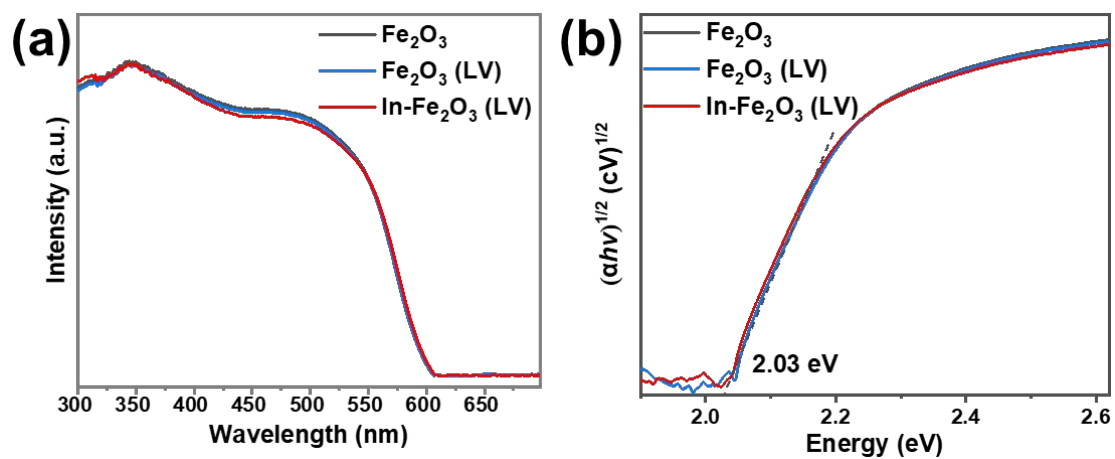


**Figure S16.** (a) UV-visible absorption spectra and (b) the derived Tauc plots of Fe<sub>2</sub>O<sub>3</sub>, Fe<sub>2</sub>O<sub>3</sub> (LV) and In-Fe<sub>2</sub>O<sub>3</sub> (LV).

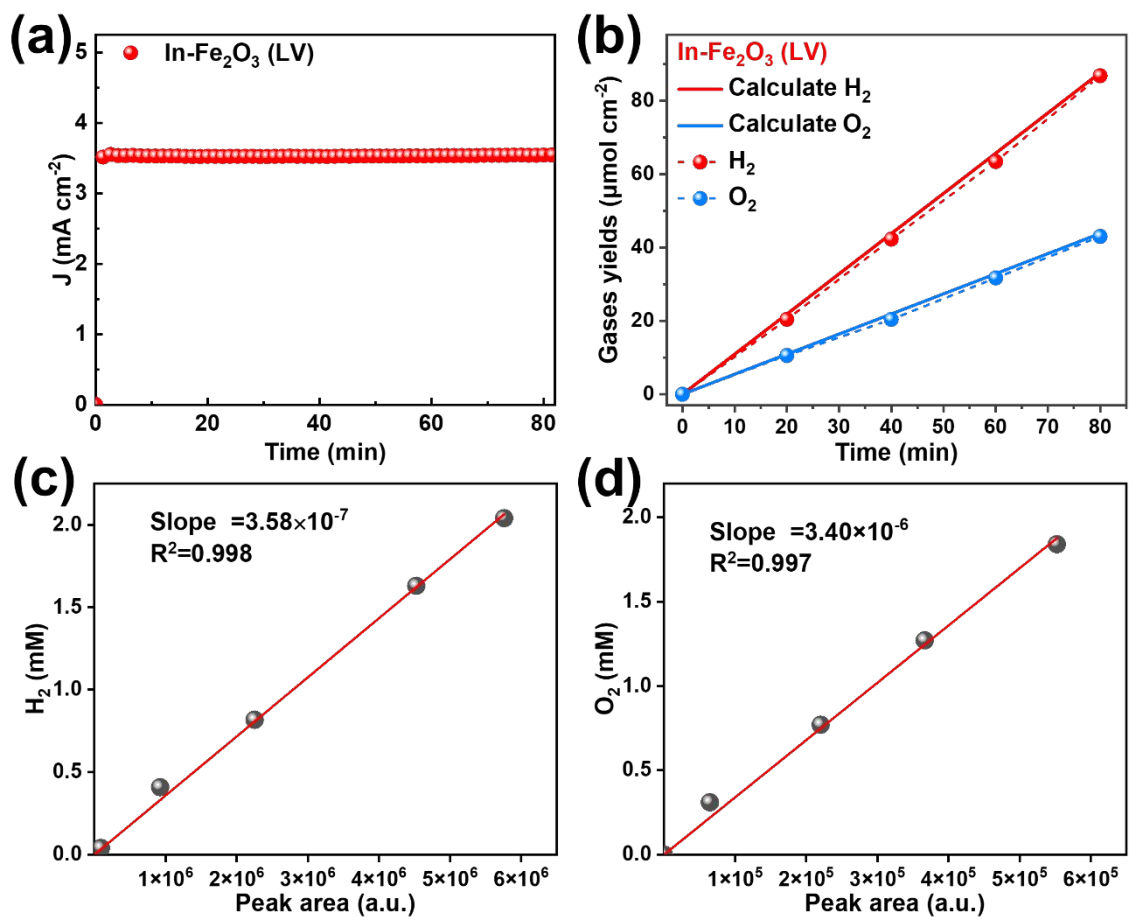


**Figure S17.** (a) I-t curve used for Faradaic efficiency and (b) H<sub>2</sub> and O<sub>2</sub> evolution curves using In-Fe<sub>2</sub>O<sub>3</sub> (LV) as the photoanode. (c) The calibration curve between the peak area and amount of H<sub>2</sub>. (d) The calibration curve between the peak area and amount of O<sub>2</sub>.

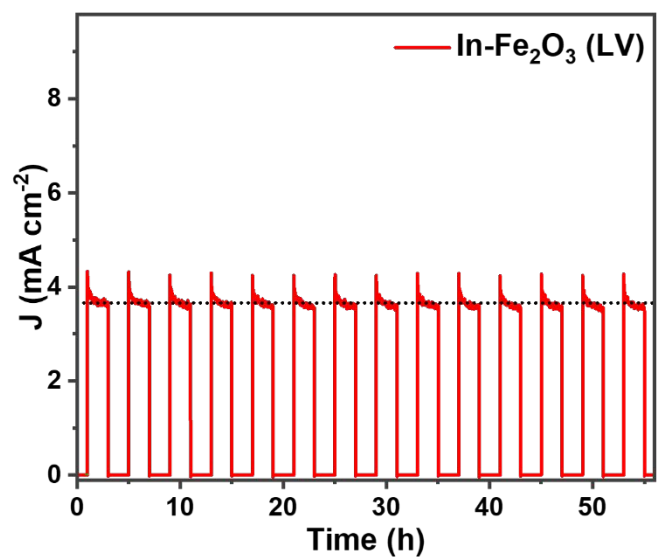


**Figure S18.** Chopped light chronoamperometry curve of In-Fe<sub>2</sub>O<sub>3</sub> (LV) at 1.23 V<sub>RHE</sub>.

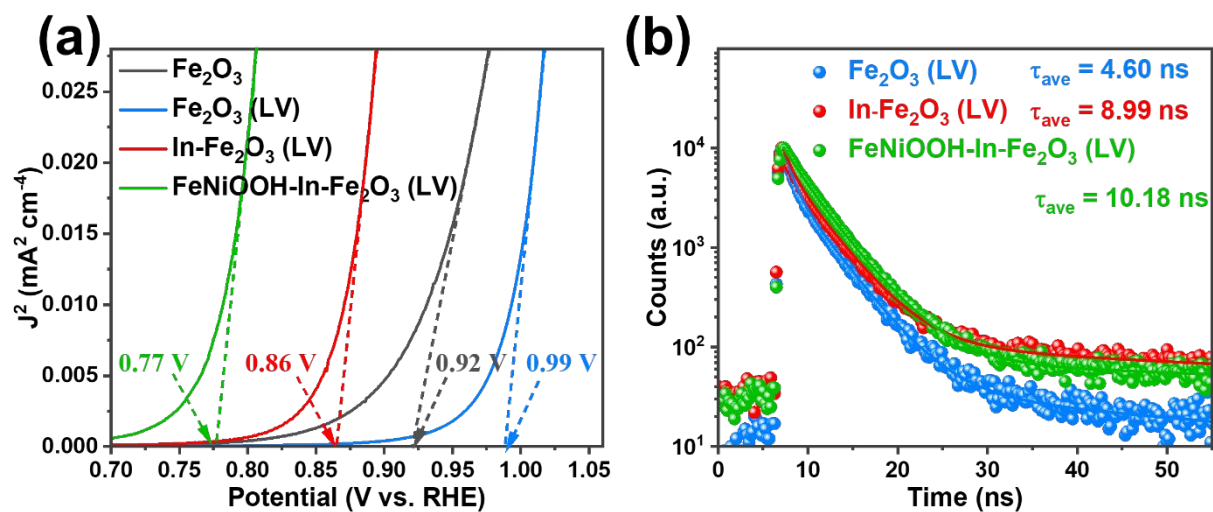


**Figure S19.** (a) Enlarged  $J^2$ - $V$  curves of Fe<sub>2</sub>O<sub>3</sub>, Fe<sub>2</sub>O<sub>3</sub> (LV), In-Fe<sub>2</sub>O<sub>3</sub> (LV) and FeNiOOH-In-Fe<sub>2</sub>O<sub>3</sub> (LV). (b) TRPL of Fe<sub>2</sub>O<sub>3</sub> (LV), In-Fe<sub>2</sub>O<sub>3</sub> (LV) and FeNiOOH-In-Fe<sub>2</sub>O<sub>3</sub> (LV).

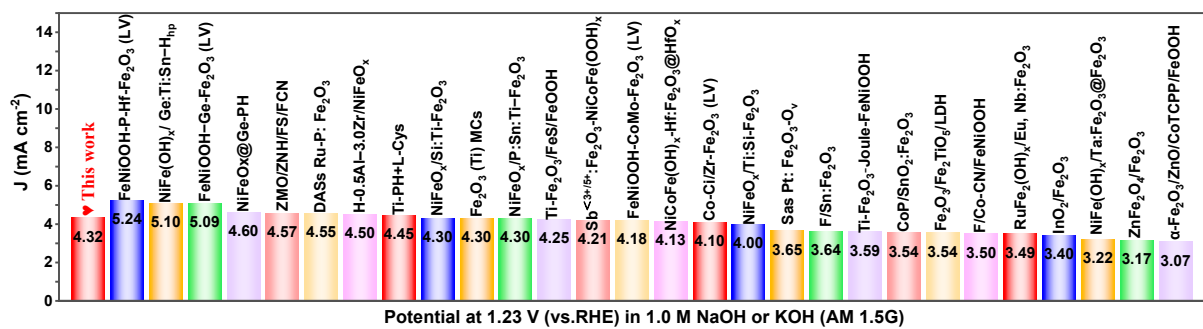
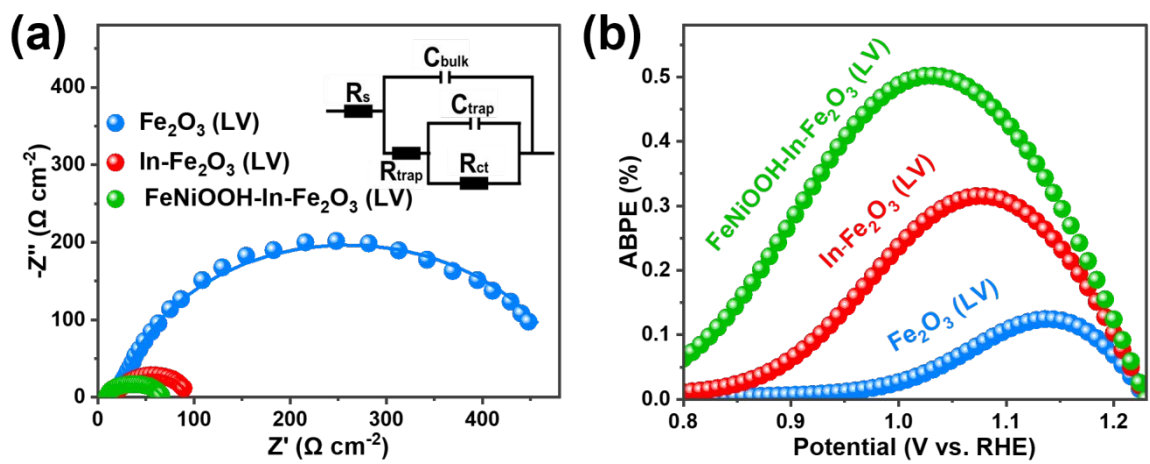
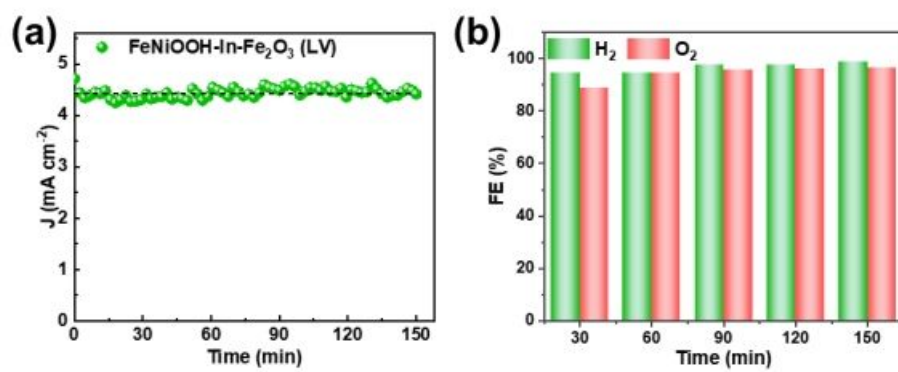


Figure S20. PEC performance comparison for hematite-based photoanodes (at 1.23 V<sub>RHE</sub>).



**Figure S21.** (a) PEIS spectra and (b) ABPE of  $\text{Fe}_2\text{O}_3$  (LV),  $\text{In-Fe}_2\text{O}_3$  (LV) and  $\text{FeNiOOH-In-Fe}_2\text{O}_3$  (LV).



**Figure S22.** (a) I-t curve used for Faradaic efficiency and (b) Faradaic efficiencies (FEs) of FeNiOOH-In-Fe<sub>2</sub>O<sub>3</sub> (LV) at 1.23 V<sub>RHE</sub>.

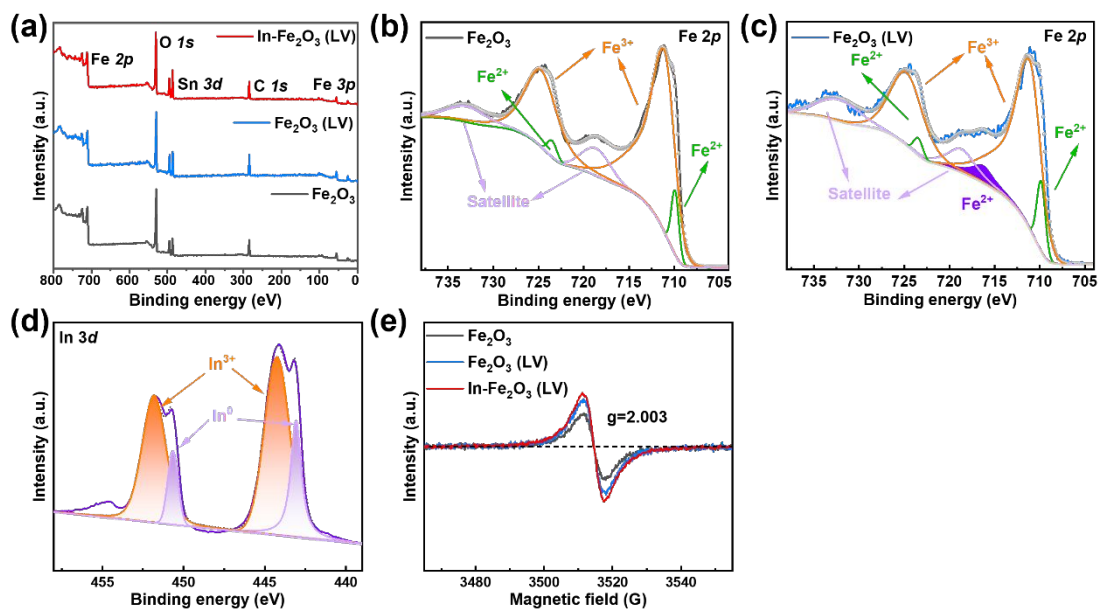


**Figure S23.** (a) XPS survey scans of  $\text{Fe}_2\text{O}_3$ ,  $\text{Fe}_2\text{O}_3$  (LV) and  $\text{In-Fe}_2\text{O}_3$  (LV). High-resolution spectra at Fe  $2p$  of  $\text{Fe}_2\text{O}_3$  (b) and  $\text{Fe}_2\text{O}_3$  (LV) (c). High-resolution spectrum of  $\text{In}_2\text{O}_3/\text{In}$  reference at In  $3d$  (d). (e) The EPR data of  $\text{Fe}_2\text{O}_3$ ,  $\text{Fe}_2\text{O}_3$  (LV) and  $\text{In-Fe}_2\text{O}_3$  (LV).

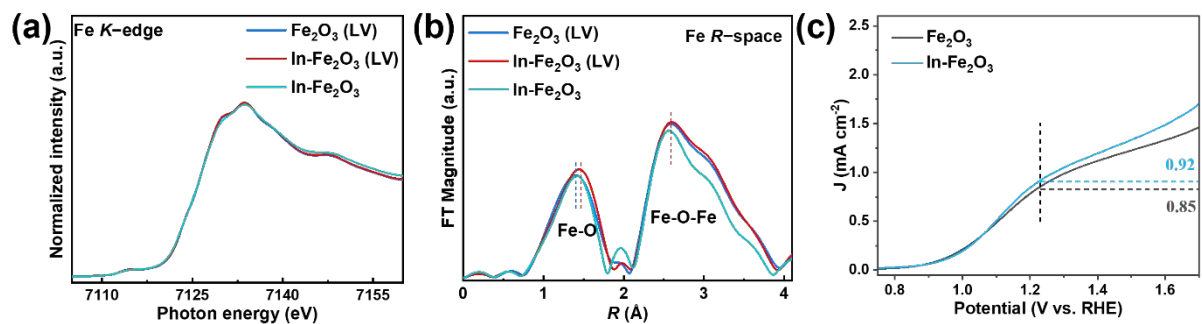


**Figure S24.** (a) Fe  $K$ -edge XANES spectra and (b)  $k^3$ -weighted Fourier-transform spectra from EXAFS for  $\text{Fe}_2\text{O}_3$ ,  $\text{In-Fe}_2\text{O}_3$ ,  $\text{Fe}_2\text{O}_3$  (LV) and  $\text{In-Fe}_2\text{O}_3$  (LV). (c)  $J$ - $V$  curves of  $\text{Fe}_2\text{O}_3$  and  $\text{In-Fe}_2\text{O}_3$ .

**Table S1.** Parameters of the equivalent circuit elements.

	$R_s$ ( $\Omega$ )	$C_{\text{bulk}}$ ( $\mu\text{F}$ )	$R_{\text{trap}}$ ( $\Omega$ )	$C_{\text{trap}}$ ( $\mu\text{F}$ )	$R_{\text{ct}}$ ( $\Omega$ )
$\text{Fe}_2\text{O}_3$	12.1 $\pm$ 0.1	25.6 $\pm$ 1.2	109.6 $\pm$ 1.9	278.6 $\pm$ 7.1	354.1 $\pm$ 4.0
$\text{Fe}_2\text{O}_3$ (LV)	11.2 $\pm$ 0.1	332.3 $\pm$ 63.1	29.1 $\pm$ 3.6	324.9 $\pm$ 53.6	460.7 $\pm$ 4.8
In- $\text{Fe}_2\text{O}_3$ (LV)	9.7 $\pm$ 0.1	412.2 $\pm$ 65.5	26.8 $\pm$ 2.2	607.8 $\pm$ 61.4	58.0 $\pm$ 2.0
FeNiOOH-In- $\text{Fe}_2\text{O}_3$ (LV)	9.5 $\pm$ 0.1	137.0 $\pm$ 8.4	34.0 $\pm$ 1.2	1671.0 $\pm$ 103.2	23.0 $\pm$ 1.3

**Table S2.** Comparison of the photocurrents on hematite-based photoanodes (at 1.23 V<sub>RHE</sub>).

Electrodes	Solutions	J (mA cm <sup>-2</sup> )	Reference
FeNiOOH-In-Fe <sub>2</sub> O <sub>3</sub> (LV)	1 M NaOH (pH 13.6)	4.32	This work
FeNiOOH-P-Hf-Fe <sub>2</sub> O <sub>3</sub> (LV)	1 M NaOH (pH 13.6)	5.24	1
NiFe(OH) <sub>x</sub> / Ge:Ti:Sn-H <sub>hp</sub>	1 M NaOH (pH 13.6)	5.10	4
FeNiOOH-Ge-Fe <sub>2</sub> O <sub>3</sub> (LV)	1 M NaOH (pH 13.6)	5.09	5
NiFeO <sub>x</sub> @Ge-PH	1 M NaOH (pH 13.6)	4.60	6
ZMO/ZNH/FS/FCN	1 M KOH (pH 13.6)	4.57	7
DASs Ru-P:Fe <sub>2</sub> O <sub>3</sub>	1 M KOH (pH 13.6)	4.55	8
H-0.5Al-3.0Zr/NiFeO <sub>x</sub>	1 M NaOH (pH 13.6)	4.50	9
Ti-PH+L-Cys	1 M NaOH (pH 13.6)	4.45	10
NiFeO <sub>x</sub> /Si:Ti-Fe <sub>2</sub> O <sub>3</sub>	1 M NaOH (pH 13.6)	4.30	11
Fe <sub>2</sub> O <sub>3</sub> (Ti) MCs	1 M NaOH (pH 13.6)	4.30	12
NiFeO <sub>x</sub> /P:Sn:Ti-Fe <sub>2</sub> O <sub>3</sub>	1 M NaOH (pH 13.6)	4.30	13
Ti-Fe <sub>2</sub> O <sub>3</sub> /FeS/FeOOH	1 M KOH (pH 13.6)	4.25	14
Sb <sup>&lt;3+</sup> /Sb <sup>5+</sup> :Fe <sub>2</sub> O <sub>3</sub> p-n homojunction-NiCoFe(OOH) <sub>x</sub>	1 M NaOH (pH 13.6)	4.21	3
FeNiOOH-CoMo-Fe <sub>2</sub> O <sub>3</sub> (LV)	1 M NaOH (pH 13.6)	4.18	15
NiCoFe(OH) <sub>x</sub> -Hf:Fe <sub>2</sub> O <sub>3</sub> @HfO <sub>x</sub>	1 M NaOH (pH 13.6)	4.13	16
Co-Ci/Zr-Fe <sub>2</sub> O <sub>3</sub> (LV)	1 M NaOH (pH 13.6)	4.10	17
NiFeO <sub>x</sub> /Ti:Si-Fe <sub>2</sub> O <sub>3</sub> (Dual photoanode)	1 M NaOH (pH 13.6)	4.00	18
Sas Pt: Fe <sub>2</sub> O <sub>3</sub> -O <sub>v</sub>	1 M KOH (pH 13.6)	3.65	19
F/Sn: Fe <sub>2</sub> O <sub>3</sub>	1 M NaOH (pH 13.6)	3.64	20

Ti-Fe <sub>2</sub> O <sub>3</sub> -Joule-FeNiOOH	1 M NaOH (pH 13.6)	3.59	21
CoP/SnO <sub>2</sub> :Fe <sub>2</sub> O <sub>3</sub>	1 M NaOH (pH 13.6)	3.54	22
Fe <sub>2</sub> O <sub>3</sub> /Fe <sub>2</sub> TiO <sub>5</sub> /LDH	1 M NaOH (pH 13.6)	3.54	23
F/Co-CN/FeNiOOH	1 M KOH (pH 13.6)	3.50	24
RuFe <sub>2</sub> (OH) <sub>x</sub> /Eu, Nb:Fe <sub>2</sub> O <sub>3</sub>	1 M NaOH (pH 13.6)	3.49	25
InO <sub>2</sub> layer/Fe <sub>2</sub> O <sub>3</sub>	1 M NaOH (pH 13.6)	3.40	26
NiFe(OH) <sub>x</sub> /Ta:Fe <sub>2</sub> O <sub>3</sub> @Fe <sub>2</sub> O <sub>3</sub>	1 M NaOH (pH 13.6)	3.22	27
ZnFe <sub>2</sub> O <sub>4</sub> /Fe <sub>2</sub> O <sub>3</sub>	1 M NaOH (pH 13.6)	3.17	28
α-Fe <sub>2</sub> O <sub>3</sub> /ZnO/CoTCPP/FeOOH	1 M NaOH (pH 13.6)	3.07	29

**Table S3.** The XPS fitting parameters of In-Fe<sub>2</sub>O<sub>3</sub> (LV), Fe<sub>2</sub>O<sub>3</sub> (LV), Fe<sub>2</sub>O<sub>3</sub> and In<sub>2</sub>O<sub>3</sub>/In.

		Binding energy (eV)			
Fe <sub>2</sub> O <sub>3</sub>	Fe <sup>2+</sup> 2p	Fe 2p <sub>3/2</sub>	Fe 2p <sub>1/2</sub>	Fe 2p	
		709.9	723.5	/	
	Fe <sup>3+</sup> 2p	Fe 2p <sub>3/2</sub>	Fe 2p <sub>1/2</sub>	satellite	
		711.1	724.7	718.7	732.9
	O 1s	O <sub>L</sub>	O <sub>V</sub>	O <sub>OH</sub>	
		529.9	531.1	532.4	
Fe <sub>2</sub> O <sub>3</sub> (LV)	Fe <sup>2+</sup> 2p	Fe 2p <sub>3/2</sub>	Fe 2p <sub>1/2</sub>	Fe 2p	
		709.9	723.5	716.3	
	Fe <sup>3+</sup> 2p	Fe 2p <sub>3/2</sub>	Fe 2p <sub>1/2</sub>	satellite	
		711.1	724.7	718.7	732.3
	O 1s	O <sub>L</sub>	O <sub>V</sub>	O <sub>OH</sub>	
		529.9	531.1	532.4	
In-Fe <sub>2</sub> O <sub>3</sub> (LV)	Fe <sup>2+</sup> 2p	Fe 2p <sub>3/2</sub>	Fe 2p <sub>1/2</sub>	Fe 2p	
		709.8	723.6	716.0	
	Fe <sup>3+</sup> 2p	Fe 2p <sub>3/2</sub>	Fe 2p <sub>1/2</sub>	satellite	
		711.0	724.9	718.7	732.8
	O 1s	O <sub>L</sub>	O <sub>V</sub>	O <sub>OH</sub>	
		529.9	531.1	532.4	
	In <sup>3+</sup> 3d	In 3d <sub>5/2</sub>		In 3d <sub>3/2</sub>	
444.2		451.7			
In <sub>2</sub> O <sub>3</sub> /In	In <sup>0</sup> 3d	In 3d <sub>5/2</sub>		In 3d <sub>3/2</sub>	
		443.1		450.6	
	In <sup>3+</sup> 3d	In 3d <sub>5/2</sub>		In 3d <sub>3/2</sub>	
		444.2		451.8	

## References

- [1] C. Lu; D. Zhang; Z. Wu; X. Zhao; K. Feng; G. Zhang; S. Wang; Z. Kang; J. Zhong, *Appl. Catal. B-Environ.* 2023, 331, 122695.
- [2] B. Klahr; S. Gimenez; F. Fabregat-Santiago; T. Hamann; J. Bisquert, *J. Am. Chem. Soc.* 2012, 134, 4294-4302.
- [3] C. Xu; H. Wang; H. Guo; K. Liang; Y. Zhang; W. Li; J. Chen; J. S. Lee; H. Zhang, *Nat. Commun.* 2024, 15, 9712.
- [4] J. Park; K.-Y. Yoon; B. G. Ghule; H. Kim; J.-H. Jang, *ACS Energy Lett.* 2024, 9, 3169-3176.
- [5] C. Lu; K. Feng; C. Li; J. Xu; S. Li; Y. Feng; Y. Zhu; S. Wang; J. Zhong, *ACS Materials Lett.* 2024, 6, 1571-1580.
- [6] K.-Y. Yoon; J. Park; M. Jung; S.-G. Ji; H. Lee; J. H. Seo; M.-J. Kwak; S. Il Seok; J. H. Lee; J.-H. Jang, *Nat. Commun.* 2021, 12, 4309.
- [7] S. Jiang; L. Ding; D. Liu; G. Wang; R. Tao; Z. Chu; X. Fan; J. Guan, *J. Mater. Chem. A* 2025, 13, 12500.
- [8] R. T. Gao; L. Liu; Y. Li; Y. Yang; J. He; X. Liu; X. Zhang; L. Wang; L. Wu, *P. Natl. Acad. Sci. USA* 2023, 120, e2300493120.
- [9] N. C. Verissimo; F. A. Pires; I. Rodríguez-Gutiérrez; J. Bettini; T. E. R. Fiuza; C. A. Biffe; F. E. Montoro; G. R. Schleder; R. H. R. Castro; E. R. Leite; F. L. Souza, *J. Mater. Chem. A* 2024, 12, 6280-6293.
- [10] L. Zhu; Z. Li; Y. Cheng; X. Zhang; H. Du; C. Zhu; D. Jiang; Y. Yuan, *Int. J. Hydrogen Energ.* 2023, 48, 32699-32707.
- [11] K.-Y. Yoon; J. Park; H. Lee; J. H. Seo; M.-J. Kwak; J. H. Lee; J.-H. Jang, *ACS Catal.* 2022, 12, 5112-5122.
- [12] Z. Zhang; H. Nagashima; T. Tachikawa, *Angew. Chem. Int. Ed.* 2020, 59, 9047-9054.
- [13] J. Kang; B. G. Ghule; S. G. Gyeong; S.-J. Ha; J.-H. Jang, *ACS Catal.* 2024, 14, 10355-10364.
- [14] S. Jiang; M. Cheng; D. Liu; R. Tao; Z. Chu; X. Fan; J. Guan, *Chem. Eng. J.* 2025, 504,

158993.

- [15] G. Zhang; C. Lu; C. Li; S. Li; X. Zhao; K. Nie; J. Wang; K. Feng; J. Zhong, *Physical Chemistry Chemical Physics* 2023, 25, 13410-13416.
- [16] W. Li; H. Guo; C. Xu; C. Tang; J. S. Lee; H. Zhang, *Appl. Catal. B-Environ.* 2024, 342, 123465.
- [17] C. Li; C. Lu; Y. Zhu; S. Li; Y. Feng; Y. Yang; B. Xu; K. Feng; J. Zhong, *Chem. Eng. J.* 2024, 486, 150120.
- [18] J. Park; K.-Y. Yoon; T. Kim; H. Jang; M.-J. Kwak; J. Y. Kim; J.-H. Jang, *Nano Energy* 2020, 76, 105089.
- [19] R. T. Gao; J. Zhang; T. Nakajima; J. He; X. Liu; X. Zhang; L. Wang; L. Wu, *Nat. Commun.* 2023, 14, 2640.
- [20] N. D. Quang; P. C. Van; D. D. Le; S. Majumder; N. D. Chinh; J.-R. Jeong; C. Kim; D. Kim, *Appl. Surf. Sci.* 2021, 558, 149898.
- [21] J. Deng; G. Li; D. Yan; W. Zhang; K. Feng; K. Nie; C. Liu; X. Lv; J. Zhong, *ACS Catal.* 2024, 14, 10635-10647.
- [22] N. D. Quang; W. Hu; H. S. Chang; P. C. Van; D. D. Viet; J.-R. Jeong; D. B. Seo; E. T. Kim; C. Kim; D. Kim, *Chem. Eng. J.* 2021, 417, 129278.
- [23] J. C. N. Fouemina; G. Li; X. She; D. Yan; X. Lv; K. Nie; J. Deng; H. Xu, *Small* 2023, 19, 2301114.
- [24] T. H. Jeon; C. Park; U. Kang; G.-h. Moon; W. Kim; H. Park; W. Choi, *Appl. Catal. B-Environ.* 2024, 340, 123167.
- [25] C. Xu; H. Wang; K. Liang; Y. Zhang; W. Li; H. Zhang, *J. Mater. Chem. A* 2024, 12, 11831-11840.
- [26] S.-S. Yi; Z.-Y. Wang; H.-M. Li; Z. Zafar; Z.-T. Zhang; L.-Y. Zhang; D.-L. Chen; Z.-Y. Liu; X.-Z. Yue, *Appl. Catal. B-Environ.* 2021, 283, 119649.
- [27] H. Zhang; D. Li; W. J. Byun; X. Wang; T. J. Shin; H. Y. Jeong; H. Han; C. Li; J. S. Lee, *Nat. Commun.* 2020, 11, 4622.
- [28] X. Hu; J. Huang; Y. Cao; B. He; X. Cui; Y. Zhu; Y. Wang; Y. Chen; Y. Yang; Z. Li; X. Liu, *Carbon Energy* 2023, 5, e369.

- [29] H. Xie; Y. Song; Y. Jiao; L. Gao; S. Shi; C. Wang; J. Hou, *ACS Nano* 2024, 18, 5712-5722.